JCTC Journal of Chemical Theory and Computation

Article

Cite This: J. Chem. Theory Comput. XXXX, XXX, XXX−XXX

pubs.acs.org/JCTC

Core-Level Binding Energies from *GW*: An Efficient Full-Frequency Approach within a Localized Basis

Dorothea Golze,[*,†,‡] Jan Wilhelm,[§,▽] Michiel J. van Setten,[∥,⊥] and Patrick Rinke[†]

[†]Department of Applied Physics, Aalto University, Otakaari 1, FI-02150 Espoo, Finland

[‡]Department of Electrical Engineering and Automation, Aalto University, PO Box 13500, 00076 Aalto, Finland

[§]Department of Chemistry, University of Zurich, Winterthurerstrasse 190, CH-8057 Zurich, Switzerland

[∥]Nanoscopic Physics, Institute of Condensed Matter and Nanosciences, Université Catholique de Louvain, 1348 Louvain-la-Neuve, Belgium

Supporting Information

ABSTRACT: The *GW* method is routinely used to predict charged valence excitations in molecules and solids. However, the numerical techniques employed in the most efficient *GW* algorithms break down when computing core excitations as measured by X-ray photoelectron spectroscopy (XPS). We present a full-frequency approach on the real axis using a localized basis to enable the treatment of core levels in *GW*. Our scheme is based on the contour deformation technique and allows for a precise and efficient calculation of the self-energy, which has a complicated pole structure for core states. The accuracy of our method is validated by comparing to a fully analytic *GW* algorithm. Furthermore, we report the obtained core-level binding energies and their deviations from experiment for a set of small molecules and large polycyclic hydrocarbons. The core-level excitations computed with our *GW* approach deviate by less than 0.5 eV from the experimental reference. For comparison, we also report core-level binding energies calculated by density functional theory (DFT)-based approaches such as the popular delta self-consistent field (ΔSCF) method. Our implementation is optimized for massively parallel execution, enabling the computation of systems up to 100 atoms.

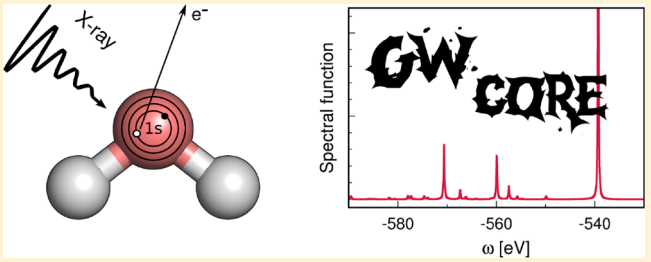

1. INTRODUCTION

Core-level spectroscopy is a powerful tool to study adsorption processes at surfaces and to investigate the chemical structure of complex materials, molecules, or liquids.[1,2] Atomic core levels are sensitive to the atomic environment, such as covalent bonding, hybridization, or the oxidation state.[3−5] The binding energies of the core electrons can be measured by X-ray photoelectron spectroscopy (XPS). Since the energetic differences (chemical shifts) between atomic core levels of the same type are often smaller than the experimental resolution, a fitting procedure is required to resolve hidden and overlapping peaks.[6,7] Peak fitting is an increasingly sophisticated and error-prone task for large molecules.[8] Accurate simulation tools to reproduce XPS spectra are thus important to support the interpretation of experimental results. To distinguish 1s excitations of second-row elements in different chemical environments, the accuracy needs to be generally better than 0.5 eV. For carbon 1s, in particular, an accuracy of the order of 0.1 eV is often required; see, for example, refs 9−11 for typical chemical shifts in organic molecules.

Currently, computational XP core-level spectroscopy is based almost exclusively on Kohn−Sham density functional theory (KS-DFT).[12,13] Although computationally efficient, DFT-based approaches are often not accurate or consistent enough to resolve XPS spectra. The workhorse of electronic structure simulations, KS-DFT, fails to reproduce the spectroscopic properties of solids[14−16] and molecules.[17,18] For the highest occupied molecular orbital (HOMO), the first ionization potential (IP) can be rigorously assigned to the negative of the KS orbital energy.[19,20] This is not the case for the other KS states. However, it is common practice, because of their conceptual similarity[21,22] to their Hartree−Fock (HF) counterparts that fulfill Koopmans' theorem.[23] The observed deviations of the KS eigenvalues from experiment are in the range of several eV for the valence states,[24] but increase to 10−30 eV for core excitations.[25]

Relating the IPs directly to the orbital energies neglects orbital relaxation effects upon the removal of an electron. These orbital readjustments can be included by means of the delta self-consistent field (ΔSCF) approach,[26] which is the state-of-the-art method for core excitations.[27] In ΔSCF, the excitation energy is calculated as the energy difference between the neutral and the ionized system. Generally, the predicted relative core-level binding energies (BEs), i.e., the shifts of the BEs with respect to a reference molecule, agree well with

Received: May 11, 2018
Published: August 9, 2018

DOI: 10.1021/acs.jctc.8b00458
J. Chem. Theory Comput. XXXX, XXX, XXX−XXX

experiment. The deviations from the experimental shifts are of the order of 0.2−0.3 eV for small molecules,[28] which is well within or close to the chemical resolution required to resolve most XPS spectra. The computed relative BEs show also little variation with respect to the exchange-correlation (XC) potential.[28] However, absolute core-level BEs computed with the ΔSCF approach depend considerably on the choice of the XC functional and can deviate from experiment by up to 2 eV.[29] The accurate calculation of absolute core excitations is important to support the alignment of complex spectra of large molecules, where peak fitting procedures become fairly biased and are based on a multitude of assumptions, such as the total number of fitted peaks.

To describe core excitations in ΔSCF, the core hole must be constrained in a particular state, which can be difficult,[30−33] in particular, when relativistic effects become important, e.g., for *p*-electrons.[34] In addition, the ΔSCF method has several conceptual problems limiting its applicability. One of them is how to treat systems with periodic boundary conditions, such as molecules on surfaces, where retaining a zero net charge in the calculation is a necessity. In this case, the ΔSCF approach can only be applied in an approximate manner, e.g., by introducing a compensating background charge or employing pseudopotential-based approaches.[35−37] For systems with localized charges, the ΔSCF approach cannot be applied at all. An example are organic salts such as ionic liquids. When generating a core hole at the cation, the negative charge at the anion would be displaced during the SCF and neutralize the core hole at the now-doubly charged cation.

A promising method to improve upon the shortcomings of ΔSCF is the *GW* approximation to many-body perturbation theory.[38] The central object of the *GW* method is the Green's function *G*, where the poles of *G* correspond to the quasiparticle (QP) excitation energies as measured in photoemission experiments. *GW* is based on a perturbative expansion in the screened Coulomb interaction *W*, as formulated by Hedin in the 1960s,[39] and accounts for nonlocal frequency-dependent screening between the electrons. Green's function theory in the *GW* approximation has become the method of choice for the computation of addition and removal energies of valence electrons in solids[40−51] and is now increasingly being applied to the valence excitations of molecules.[24,52−59] For the latter, average deviations of less than 0.2 eV from the coupled cluster singles, doubles, and perturbative triples [CCSD(T)] reference values have been reported.[60,61] Mean absolute errors for the first IP are even below 0.1 eV when comparing vibrationally resolved *GW* spectra to experiment.[62] For core excitations, we are only aware of two exploratory *GW* studies for solids that report partly promising agreement with experiment.[63,64] However, a recent investigation using the established *GW* procedures for valences states found large deviations (up to 10 eV) for molecular core levels.[25]

This motivated us to advance the *GW* method for molecular core excitations within first-order perturbation G_0W_0. The requirements for a core-level implementation are 2-fold:

(1) The core electrons have to be described explicitly. Localized basis sets are the best choice for this task since they can be tailored to model the rapid oscillations of the wave function in the vicinity of the atomic nuclei. Many *GW* implementations,[46,65−67] however, employ plane wave expansions of the electronic density in combination with frozen core approximations prohibiting assessment of core excitations by design.

(2) The self-energy, which describes the electron−electron interactions in *GW*, has a more complicated structure in the core than in the valence region, which we will demonstrate in this work. Therefore, it is crucial to compute the self-energy in a numerically stable manner.

In this work, we account for both requirements (1) and (2) by an efficient and accurate full-frequency implementation on the real frequency axis using atom-centered basis functions.

This paper is organized as follows. After briefly introducing the G_0W_0 approach and recalling the basic equations for computing G_0 and W_0, we summarize the equations for the resolution-of-the-identity (RI) approach in section 3. We then apply the RI approach in section 4 and derive the working expressions used in our implementation and introduce the spectral function in section 5. Implementation and computational details are described in sections 6 and 7. We discuss self-energy structures and spectral functions and the accuracy of our implementation for small- and medium-sized molecular structures in section 8. After reporting the computational efficiency we finally draw conclusions in section 9.

2. QUASIPARTICLE ENERGIES FROM G_0W_0

Introducing *GW* by analogy to DFT, the XC potential v^{xc} of DFT is replaced by a self-energy Σ. The KS equations then transform to a set of self-consistent quasiparticle equations, which can be solved iteratively. In practice, *GW* calculations are often performed on top of an underlying DFT or HF calculation. Such single-shot perturbation calculations are referred to as G_0W_0. The corrections to the KS-DFT orbital energies ϵ_n of a molecular orbital (MO) ψ_n are then given by

$$\epsilon_n^{G_0W_0} = \epsilon_n + \mathrm{Re}\Sigma_n(\epsilon_n^{G_0W_0}) - v_n^{xc} \tag{1}$$

where we introduced the (n, n)-diagonal matrix elements of the exchange-correlation potential, $v_n^{xc} = \langle\psi_n|v^{xc}|\psi_n\rangle$, and the self-energy,

$$\Sigma_n(\omega) = \langle\psi_n|\Sigma(\omega)|\psi_n\rangle \tag{2}$$

Note that the spin has been omitted for the sake of simplicity, but can easily be reintroduced. The self-energy is given by[68]

$$\Sigma(\mathbf{r}, \mathbf{r}', \omega) = \frac{i}{2\pi}\int d\omega' G_0(\mathbf{r}, \mathbf{r}', \omega + \omega')W_0(\mathbf{r}, \mathbf{r}', \omega')\exp(i\omega'\eta) \tag{3}$$

where G_0 is the noninteracting KS Green's function, W_0 the screened Coulomb interaction, and η a positive infinitesimal. The KS Green's function is given by

$$G_0(\mathbf{r}, \mathbf{r}', \omega) = \sum_m \frac{\psi_m(\mathbf{r})\psi_m(\mathbf{r}')}{\omega - \epsilon_m - i\eta\ \mathrm{sgn}(\epsilon_F - \epsilon_m)} \tag{4}$$

where ϵ_F denotes the Fermi energy. In eq 4, the sum includes all occupied and virtual KS orbitals ψ_m with the corresponding KS orbital energies ϵ_m. The screened Coulomb interaction at the random phase approximation (RPA) level is defined as

$$W_0(\mathbf{r}, \mathbf{r}', \omega) = \int d\mathbf{r}''\varepsilon^{-1}(\mathbf{r}, \mathbf{r}'', \omega)v(\mathbf{r}'', \mathbf{r}') \tag{5}$$

with the dielectric function ε and the bare Coulomb interaction $v(\mathbf{r}, \mathbf{r}') = 1/|\mathbf{r} - \mathbf{r}'|$. The dynamical dielectric function is

DOI: 10.1021/acs.jctc.8b00458
J. Chem. Theory Comput. XXXX, XXX, XXX−XXX

$$\varepsilon(\mathbf{r}, \mathbf{r}', \omega) = \delta(\mathbf{r}, \mathbf{r}') - \int d\mathbf{r}'' v(\mathbf{r}, \mathbf{r}'') \chi_0(\mathbf{r}'', \mathbf{r}', \omega) \tag{6}$$

where the real-space Adler–Wiser representation[69,70] of the irreducible polarizability χ_0 reads[68]

$$\chi_0(\mathbf{r}, \mathbf{r}', \omega) = \sum_i^{\text{occ}} \sum_a^{\text{virt}} \psi_a(\mathbf{r}')\psi_i(\mathbf{r}')\psi_i(\mathbf{r})\psi_a(\mathbf{r}) \times \left\{ \frac{1}{\omega - (\epsilon_a - \epsilon_i) + i\eta} + \frac{1}{-\omega - (\epsilon_a - \epsilon_i) + i\eta} \right\} \tag{7}$$

The index i refers to an occupied MO and a refers to a virtual one.

The self-energy $\Sigma = \Sigma^c + \Sigma^x$ has a correlation contribution Σ^c and an exchange contribution Σ^x. The latter is not dependent on the frequency and is given by

$$\Sigma^x(\mathbf{r}, \mathbf{r}') = -\sum_i^{\text{occ}} \psi_i(\mathbf{r})\psi_i(\mathbf{r}')v(\mathbf{r}, \mathbf{r}') \tag{8}$$

The QP energies $\epsilon_n^{G_0W_0}$ calculated from G_0W_0 are dependent on the reference ground state encoded in G_0 and W_0.[71] Different methods to optimize the DFT starting point have been successfully employed to obtain accurate valence excitations.[72,73]

3. RI APPROXIMATION

The four-center electron repulsion integrals (4c-ERIs) are of central importance for the calculation of W_0 and are defined as

$$(nm|kl) = \int d\mathbf{r}\, d\mathbf{r}' \psi_n(\mathbf{r}')\psi_m(\mathbf{r}')\psi_k(\mathbf{r})\psi_l(\mathbf{r})v(\mathbf{r}, \mathbf{r}') \tag{9}$$

The MOs $\{\psi_n\}$ are expanded in localized atom-centered orbitals $\{\phi_\mu\}$,

$$\psi_n(\mathbf{r}) = \sum_\mu C_{\mu n}\phi_\mu(\mathbf{r}) \tag{10}$$

where $C_{\mu n}$ are the MO coefficients obtained from KS-DFT. We employ the RI approximation with the Coulomb metric[74] (RI-V) to refactor the 4c-ERIs in two- and three-center integrals,

$$(nm|kl)_{\text{RI-V}} = \sum_{PQ} (nm|P)V_{PQ}^{-1}(Q|kl) \tag{11}$$

which is exact in the limit of a complete auxiliary basis set $\{\varphi_P\}$. Note that the auxiliary functions P and Q are also local and atom-centered. The two-center (2c) integrals, or, equivalently, the Coulomb matrix elements V_{PQ} are given by

$$V_{PQ} := (P|Q) = \int d\mathbf{r}\, d\mathbf{r}' \varphi_P(\mathbf{r}')\varphi_Q(\mathbf{r})v(\mathbf{r}, \mathbf{r}') \tag{12}$$

and the three-center (3c) integrals are defined as

$$(nm|P) = \sum_{\mu\nu} (\mu\nu|P)C_{\mu n}C_{\nu m} \tag{13}$$

$$(\mu\nu|P) = \int d\mathbf{r}\, d\mathbf{r}' \phi_\mu(\mathbf{r}')\phi_\nu(\mathbf{r}')\varphi_P(\mathbf{r})v(\mathbf{r}, \mathbf{r}') \tag{14}$$

The integral over the atomic orbitals, $(\mu\nu|P)$, is obtained by analytic or numeric integration, depending on the functional form of the basis functions $\{\phi_\mu\}$.

We introduce the quantity

$$M_P^{\mu\nu} = \sum_R (\mu\nu|R)V_{RP}^{-1/2} \tag{15}$$

and its transformation in the MO basis

$$O_P^{nm} = \sum_{\mu\nu} M_P^{\mu\nu} C_{\mu n} C_{\nu m} \tag{16}$$

to reformulate the RI expression for the 4c-ERIs in a more compact form,

$$(nm|kl)_{\text{RI-V}} = \sum_P O_P^{nm} O_P^{kl} \tag{17}$$

The RI-V method is a well-established technique in quantum chemistry, because of its accuracy and fast convergence, with respect to the number of auxiliary functions,[75−78] and is also commonly used in GW implementations.[24,53,79,80] In RI-V, we minimize the Coulomb repulsion of the residual, with respect to the expansion of the basis pairs $\phi_\mu\phi_\nu$ in auxiliary functions. Compared to RI with the overlap metric, the error in the residual is quadratic instead of linear.[81−83]

4. EVALUATION OF THE SELF-ENERGY

In this section, we start by briefly reviewing the popular analytic continuation (AC) method. We then derive the equations for calculating the self-energy with the contour deformation (CD) technique, which is the method that we will employ to calculate core-level excitations. In the following, we refer to G_0W_0 calculations with the first approach as AC-G_0W_0 and to calculations with the second approach as CD-G_0W_0.

4.1. Analytic Continuation (AC). On the real-frequency axis, Σ exhibits a complex structure with many poles, whereas it has a smooth form on the imaginary axis.[84,85] To avoid the complicated behavior for real frequencies, a common approach is to evaluate the self-energy in the imaginary frequency domain, where Σ is given by

$$\Sigma(\mathbf{r}, \mathbf{r}', i\omega) = -\frac{1}{2\pi} \int_{-\infty}^{\infty} d\omega' G_0(\mathbf{r}, \mathbf{r}', i\omega + i\omega')W_0(\mathbf{r}, \mathbf{r}', i\omega') \tag{18}$$

The experimental observables like QP energies and spectral functions are measured for real frequencies. This implies that $\Sigma(i\omega)$ must be analytically continued to the real axis to compute these quantities. An analytical form is obtained by fitting the matrix elements $\Sigma_n^c(i\omega)$ to a multipole model such as the popular Padé approximant, which is employed in several state-of-the-art GW implementations.[52,67,86] The approximant is given by

$$\Sigma_n(i\omega) \approx \frac{a_0 + a_1(i\omega) + \cdots + a_{(N-1)/2}(i\omega)^{(N-1)/2}}{1 + b_1(i\omega) + \cdots + b_{N/2}(i\omega)^{N/2}} \tag{19}$$

where N is the number of Padé parameters. In practice, we calculate the N-point Padé approximant using Thiele's reciprocal difference method. There, the unknown complex coefficients a_i and b_j are computed recursively from a set of imaginary frequencies $\{i\omega\}$ and the corresponding values $\Sigma(i\omega)$. We refer to ref 87 for details. The self-energy in the real-frequency domain is finally obtained by substituting $(i\omega)$ by ω in eq 19.

It has been demonstrated that the AC reproduces the structure of the self-energy well for valences states[52,84] yielding reliable results for the corresponding IPs.[18,52,53,88−90] In particular, benchmark studies[52] showed that the Padé

DOI: 10.1021/acs.jctc.8b00458
J. Chem. Theory Comput. XXXX, XXX, XXX−XXX

approximation produces more accurate results than less-flexible models such as the "two-pole fit".[84]

4.2. Contour Deformation (CD). An alternative method to compute the self-energy is to calculate the integral along the real-frequency axis in eq 3, employing the integral along the contour; see Figure 1. Using the CD technique,[91−95] we obtain

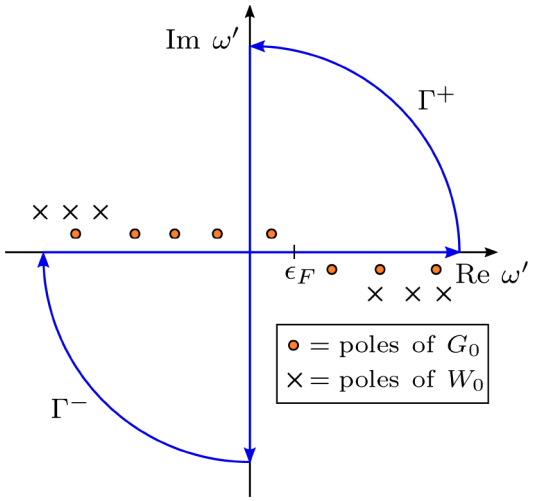

Figure 1. Contour of the integration used to evaluate $\Sigma(\omega)$. The integration contours Γ^+ and Γ^- enclose only the poles of G_0, but never the poles of W_0.

the self-energy directly on the real-frequency axis, avoiding the fitting procedure described in section 4.1. At the same time, we circumvent the numerical unstable integration on the real-frequency axis, where the poles of G_0 and W_0 are located. Since the integrals along the arcs vanish, eq 3 transforms to

$$\Sigma(\mathbf{r}, \mathbf{r}', \omega) = \frac{i}{2\pi}\oint d\omega' G_0(\mathbf{r}, \mathbf{r}', \omega + \omega')W_0(\mathbf{r}, \mathbf{r}', \omega') - \frac{1}{2\pi}\int_{-\infty}^{\infty} d\omega' G_0(\mathbf{r}, \mathbf{r}', \omega + i\omega')W_0(\mathbf{r}, \mathbf{r}', i\omega') \tag{20}$$

where the first term is the entire contour integral and the second term is the integral along the imaginary axis. For the following discussion, we introduce the notations

$$R(\omega) := \frac{i}{2\pi}\oint d\omega' G_0(\mathbf{r}, \mathbf{r}', \omega + \omega')W_0(\mathbf{r}, \mathbf{r}', \omega') \tag{21}$$

$$I(\omega) := \frac{1}{2\pi}\int_{-\infty}^{\infty} d\omega' G_0(\mathbf{r}, \mathbf{r}', \omega + i\omega')W_0(\mathbf{r}, \mathbf{r}', i\omega') \tag{22}$$

The contour integral $R(\omega)$ is calculated from the residues of the poles enclosed in the contours, i.e., in the subset of the complex planes D_{Γ^+} and D_{Γ^-} encircled by Γ^+ and Γ^-, respectively. The poles of W_0 never fall inside the contour. However, depending on ω, some poles of $G_0(\omega + \omega')$ can enter D_{Γ^+} or D_{Γ^-}. Recalling the expression for the Green's function on the real axis in eq 4, we directly find that the poles of G_0 are located at the complex frequencies

$$\omega_m' = \epsilon_m - \omega + i\eta\ \mathrm{sgn}(\epsilon_F - \epsilon_m) \tag{23}$$

For $\omega < \epsilon_F$, the poles ω_m' can only enter D_{Γ^+} as shown in Figure 1. These poles stem from occupied states. For $\omega > \epsilon_F$, the situation is reversed and poles of the unoccupied states can shift into D_{Γ^-}. Employing the residue theorem, we obtain for the contour integral defined in eq 21

$$R(\omega) = -\sum_{\omega_m' \in D_{\Gamma^+}} \mathrm{Res}\{G_0(\mathbf{r}, \mathbf{r}', \omega + \omega')W_0(\mathbf{r}, \mathbf{r}', \omega'), \omega_m'\} + \sum_{\omega_m' \in D_{\Gamma^-}} \mathrm{Res}\{G_0(\mathbf{r}, \mathbf{r}', \omega + \omega')W_0(\mathbf{r}, \mathbf{r}', \omega'), \omega_m'\} \tag{24}$$

where the residues are given by

$$\begin{aligned}&\mathrm{Res}\{G_0(\mathbf{r}, \mathbf{r}', \omega + \omega')W_0(\mathbf{r}, \mathbf{r}', \omega'), \omega_m'\}\\ &\quad = \lim_{\omega' \to \omega_m'}(\omega' - \omega_m')G_0(\mathbf{r}, \mathbf{r}', \omega + \omega')W_0(\mathbf{r}, \mathbf{r}', \omega')\\ &\quad = \psi_m(\mathbf{r})\psi_m(\mathbf{r}')W_0(\mathbf{r}, \mathbf{r}', \omega_m')\end{aligned} \tag{25}$$

By inserting the third line of eq 25 in eq 24 and using eq 23, we obtain for the diagonal matrix elements of $R(\omega)$

$$R_n(\omega) := \langle n|R(\omega)|n\rangle = \sum_m f_m W_{nm} \tag{26}$$

$$W_{nm} := \langle nm|W_0(\mathbf{r}, \mathbf{r}', \epsilon_m - \omega + i\eta\ \mathrm{sgn}(\epsilon_F - \epsilon_m))|mn\rangle \tag{27}$$

where the contribution of the residues is determined by f_m:

$$f_m = \begin{cases} +1 & \text{if} \quad \epsilon_F < \epsilon_m < \omega \\ -1 & \text{if} \quad \omega < \epsilon_m < \epsilon_F \\ 0 & \text{else} \end{cases} \tag{28}$$

From eq 28, we directly see that the residues do not contribute to the self-energy for $\epsilon_{\mathrm{HOMO}} < \omega < \epsilon_{\mathrm{LUMO}}$, where ϵ_{HOMO} and ϵ_{LUMO} are the KS orbital energies of the HOMO and lowest occupied molecular orbital (LUMO). Therefore, the residue term is zero for frequencies within the band gap.

To obtain an expression for W_{nm} in eq 27, we evaluate the irreducible polarizability χ_0 given in eq 7 at $\epsilon_m - \omega + i\eta$ for $\omega < \epsilon_m < \epsilon_F$ and $\epsilon_m - \omega - i\eta$ for $\omega > \epsilon_m > \epsilon_F$. It is easy to show that

$$\begin{aligned}\chi_0(\epsilon_m - \omega + i\eta) &= \chi_0(|\epsilon_m - \omega| + i\eta) \quad \omega < \epsilon_m < \epsilon_F\\ \chi_0(\epsilon_m - \omega - i\eta) &= \chi_0(|\epsilon_m - \omega| + i\eta) \quad \omega > \epsilon_m > \epsilon_F\end{aligned} \tag{29}$$

After inserting eqs 5−7, eq 29, and the RI approximation (eq 17) into eq 27, we obtain the following expression for the W_{nm} matrix elements:

$$W_{nm} = \sum_{PQ} O_P^{nm}[1 - \Pi(|\epsilon_m - \omega| + i\eta)]^{-1}_{PQ} O_Q^{mn} \tag{30}$$

where the representation of the polarizability in the auxiliary basis is given by

$$\Pi_{PQ}(\omega) = \sum_{ia} O_P^{ia}\left[\frac{1}{\omega - (\epsilon_a - \epsilon_i) + i\eta} + \frac{1}{-\omega - (\epsilon_a - \epsilon_i) + i\eta}\right]O_Q^{ia} \tag{31}$$

We turn now our attention to the evaluation of the integral along the imaginary axis $I(\omega)$ defined in eq 22. The expression for G_0 given in eq 4 remains unchanged, except that we substitute ω' by $i\omega'$. The same holds for W_0, ε, and χ_0, where we replace ω by $i\omega$ in eqs 5−7. Analogously to the derivation

DOI: 10.1021/acs.jctc.8b00458
J. Chem. Theory Comput. XXXX, XXX, XXX−XXX

of $R_n(\omega)$, we use again the RI approximation as formulated in eq 17 to obtain the diagonal matrix elements of $I(\omega)$ by using eqs 4−7:

$$I_n(\omega) := \langle n|I(\omega)|n\rangle = \frac{1}{2\pi}\sum_m \int_{-\infty}^{\infty} d\omega' \frac{1}{\omega + i\omega' - \epsilon_m - i\eta\ \mathrm{sgn}(\epsilon_F - \epsilon_m)} \times \sum_{PQ} O_P^{nm}[1 - \Pi(i\omega')]^{-1}_{PQ} O_Q^{mn} \tag{32}$$

The self-energy Σ_n is obtained by inserting eq 30 into eq 26 and then eqs 26 and 32 in eq 20. We finally compute the correlation self-energy Σ_n^c by subtracting the exact exchange energy Σ_n^x (eq 8) from Σ_n. The latter is equivalent to subtracting the bare Coulomb interaction v from the screened interaction W_0. This yields the correlation parts R_n^c and I_n^c of R_n (eq 26) and I_n (eq 32),

$$R_n^c(\omega) = \sum_m f_m W_{nm}^c(|\epsilon_m - \omega| + i\eta) \tag{33}$$

with

$$W_{nm}^c(|\epsilon_m - \omega| + i\eta) = \sum_{PQ} O_P^{nm}[[1 - \Pi(|\epsilon_m - \omega| + i\eta)]^{-1}_{PQ} - \delta_{PQ}]O_Q^{mn} \tag{34}$$

and

$$I_n^c(\omega) = \frac{1}{2\pi}\sum_m \int_{-\infty}^{\infty} d\omega' \frac{W_{nm}^c(i\omega')}{\omega + i\omega' - \epsilon_m - i\eta\ \mathrm{sgn}(\epsilon_F - \epsilon_m)} \tag{35}$$

with

$$W_{nm}^c(i\omega) = \sum_{PQ} O_P^{nm}[[1 - \Pi(i\omega)]^{-1}_{PQ} - \delta_{PQ}]O_Q^{mn} \tag{36}$$

Equations 33 and 35 complete the ingredients to compute the (n, n)-diagonal elements of the self-energy,

$$\Sigma_n(\omega) = \Sigma_n^x + R_n^c(\omega) - I_n^c(\omega) \tag{37}$$

which is used to compute the G_0W_0 quasiparticle energies from the QP equation (eq 1). The correlation self-energy $\Sigma_n^c := R_n^c - I_n^c$ is a complex quantity and only its real part is required to solve eq 1. However, for the computation of other observables, such as the spectral function introduced in section 5, the full complex self-energy is required. Therefore, it is important to note that, in a rigorous derivation of the CD equations, also the frequency integral term I_n^c has a minor contribution to the imaginary part of Σ_n^c. This is discussed in more detail in section 8.1.

5. SPECTRAL FUNCTION

The Green's function G for interacting electrons has its poles at the QP energies and the imaginary part of G is expected to have peaks at these energies.[68] Therefore, the spectral information can be directly retrieved from G by computing the spectral function or density of states $A(\omega)$:

$$A(\omega) = -\frac{1}{\pi}\int d\mathbf{r} \lim_{\mathbf{r}'\to\mathbf{r}} \mathrm{Im}G(\mathbf{r}, \mathbf{r}', \omega)\ \mathrm{sgn}(\omega - \epsilon_F) = -\frac{1}{\pi}\mathrm{Tr}[\mathrm{Im}G(\omega)\ \mathrm{sgn}(\omega - \epsilon_F)] \tag{38}$$

Employing the Dyson equation, $G = G_0 + G_0\Sigma G$, with the G_0W_0 self-energy Σ and omitting off-diagonal elements of Σ, we diagonalize G in the basis of KS eigenstates m,

$$G_m(\omega) = \frac{1}{[G_m^0(\omega)]^{-1} - [\Sigma_m(\omega) - v_m^{xc}]} \tag{39}$$

Using the eigenvalues G_m of G to compute the trace in eq 38 and using eqs 4 and 37 yields

$$A(\omega) = -\frac{1}{\pi}\sum_m \mathrm{Im}G_m(\omega)\ \mathrm{sgn}(\omega - \epsilon_F) \tag{40}$$

$$= -\frac{1}{\pi}\sum_m \mathrm{Im}[\omega - \epsilon_m - (\Sigma_m^c(\omega) + \Sigma_m^x - v_m^{xc})]^{-1} \times \mathrm{sgn}(\omega - \epsilon_F) \tag{41}$$

Note that we need the full complex correlation self-energy $\Sigma_m^c(\omega)$ for the evaluation of $A(\omega)$, whereas only its real part is required for solving the QP equation (eq 1). However, the spectral function yields the full spectral information and shows next to the main peaks, which correspond to the QP excitations, also smaller peaks and satellite structures due to a variety of collective phenomena.[68]

6. IMPLEMENTATION DETAILS

The CD-G_0W_0 approach has been implemented in the all-electron code FHI-aims, which is based on numerically tabulated atom-centered orbitals (NAOs).[96] In FHI-aims, the MOs are expanded in the NAO basis $\{\phi_\mu\}$, with basis functions of the form

$$\phi_\mu(\mathbf{r}) = \frac{u_\mu(r)}{r}Y_{lm}(\Omega) \tag{42}$$

where $u_\mu(r)$ are radial functions and $Y_{lm}(\Omega)$ spherical harmonics. The functions u_μ are not restricted to any particular shape, but are numerically tabulated on dense grids. Other popular local basis functions, e.g., Gaussian-type orbitals can be considered as special cases of the general form.

The pseudocode for our CD-G_0W_0 implementation is shown in Figure 2. We start by computing the 2c and 3c RI integrals V_{PQ} and $(\mu\nu|P)$. The auxiliary functions P and Q are NAOs that are generated from products of the primary basis functions; see ref 79 for details. The 2c integrals are calculated in Fourier space as described by Talman,[97,98] employing a logarithmic Bessel transform,[99] while the 3c integrals are computed by numerical integration using overlapping atom-centered spherical grids; see ref 79 for a comprehensive description. We then get the orbital energies $\{\epsilon_n\}$ and the MO coefficients $\{C_{\mu n}\}$ from an electronic structure optimization at the KS-DFT level. The RI integrals are not only used to expand the self-energy in the MO basis, but are already employed in the SCF procedure of the DFT calculation. This is the case for hybrid functionals when an efficient evaluation of the exact HF exchange is required.[79]

The QP energies are obtained by solving eq 1 iteratively; see Figure 2. To compute the self-energy, we must re-evaluate the residue term R_n^c and the integral term I_n^c at each step. The latter is calculated by numerical integration using a modified Gauss-Legendre grid[79] with $\{i\omega\}$ grid points. I_n^c is constructed by integrating over the matrix elements $W_{nm}^c(i\omega)$. Since these matrix elements are not dependent on the QP energies, they can be precomputed once when the QP cycle is initialized. The computational cost for the calculation of R_n^c is for core states

DOI: 10.1021/acs.jctc.8b00458
J. Chem. Theory Comput. XXXX, XXX, XXX−XXX

Compute $M_P^{\mu\nu} = \sum_R (\mu\nu|R) V_{RP}^{-1/2}$
Get $\{\epsilon_n\}$ and MO coefficients $\{C_{\mu n}\}$ from SCF
Transformation to MO basis: $O_P^{nm} = \sum_{\mu\nu} M_P^{\mu\nu} C_{\mu n} C_{\nu m}$
Loop over all $i\omega$
    Calculate $\Pi_{PQ}(i\omega)$ from O_P^{nm}
    Calculate $W_{nm}^c(i\omega)$ from O_P^{nm} and $\Pi_{PQ}(i\omega)$
End $i\omega$ loop
Set for state n: $\epsilon'_n = \epsilon_n$
Start QP cycle for state n
    Loop over all residues $\{\epsilon_m - \epsilon'_n\}$
        Set $\omega_{nm} = |\epsilon_m - \epsilon'_n| + i\eta$
        Calculate $\Pi_{PQ}(\omega_{nm})$ from O_P^{nm}
        Calculate $W_{nm}^c(\omega_{nm})$ from O_P^{nm} and $\Pi_{PQ}(\omega_{nm})$
        Sum up: $R_n^c(\epsilon'_n) = R_n^c(\epsilon'_n) + f_m W_{nm}^c(\omega_{nm})$
    End residue loop
    Loop over all KS states m
        Set for all $i\omega$: $k_{nm}(i\omega) = [\epsilon'_n + i\omega - \epsilon_m \pm i\eta]^{-1}$
        Sum up: $I_n^c(\epsilon'_n) = I_n^c(\epsilon'_n) + \int d\omega \frac{k_{nm}(i\omega) W_{nm}^c(i\omega)}{2\pi}$
    End m loop
    Calculate $\Sigma_n(\epsilon'_n) = \Sigma_n^x + R_n^c(\epsilon'_n) - I_n^c(\epsilon'_n)$
    Calculate QP energy: $\epsilon_n^{G_0W_0} = \epsilon_n + \mathrm{Re}\,\Sigma_n(\epsilon'_n) - v_n^{xc}$
    Set $\epsilon'_n = \epsilon_n^{G_0W_0}$
    If QP energy $\epsilon_n^{G_0W_0}$ converged exit
End QP loop

Figure 2. Pseudocode for the CD-G_0W_0 method. Displayed is the computation of the QP energy $\epsilon_n^{G_0W_0}$ for state n.

significantly higher than for valence states. The reason is that the matrix elements $W_{nm}^c(|\epsilon_m - \omega|)$ must be calculated at each QP cycle step for each pole $(\epsilon_m - \omega)$ of G that enters the contour and therefore contributes as residue. The number of residues depends on the KS state n for which the G_0W_0 correction is calculated; see eq 28. We have typically only one residue for the HOMO. However, for the energetically lowest core state, the number of residues increases to $N_{\mathrm{elec}}/2$, where N_{elec} is the number of electrons. Therefore, the computational complexity for core-level excitations is one order larger than for valence states.

An alternative to the iterative procedure is the graphical solution of eq 1. For the latter case, the self-energy matrix elements are computed and plotted on a fine grid of real frequencies $\{\omega\}$ in the region where the solution is expected. The QP energies are then obtained by graphically finding the point where the self-energy and the straight line $\omega - \epsilon_n + v_n^{xc} - \Sigma_n^x$ intersect; see eq 1. The iterative solution is computationally far more efficient since the self-energy must be calculated only for a few frequencies, i.e., for one frequency per step. Therefore, in the following, the graphical solution is not used for production calculations of QP excitations, but is used exclusively for an in-depth discussion of the solution behavior of eq 1; see section 8.2.

The CD-G_0W_0 approach is parallelized using a standard message passing interface (MPI). The matrix elements O_P^{ia} are distributed over the pairs of occupied and virtual orbitals ia to compute the polarizability in the auxiliary basis $\Pi_{PQ}(\omega)$. The latter is then redistributed over the auxiliary functions P and Q. The subsequent parallel matrix operations are performed with ScaLAPACK. We have chosen another parallelization strategy for the evaluation of the spectral function $A(\omega)$. The computation of $A(\omega)$ with a sufficient spectral resolution is only feasible for small molecules, since one frequency point requires the calculation of Σ_n^c for all KS states n. In favor of a high resolution of $A(\omega)$, we apply the distribution to the frequency points, instead of the matrix elements.

7. COMPUTATIONAL DETAILS

Core-level calculations are performed for small isolated molecules and medium-sized polycyclic aromatic hydrocarbons, such as coronene, phenanthrene, and anthrone (see Figure 3), which are stable in the gas phase. Core excitations

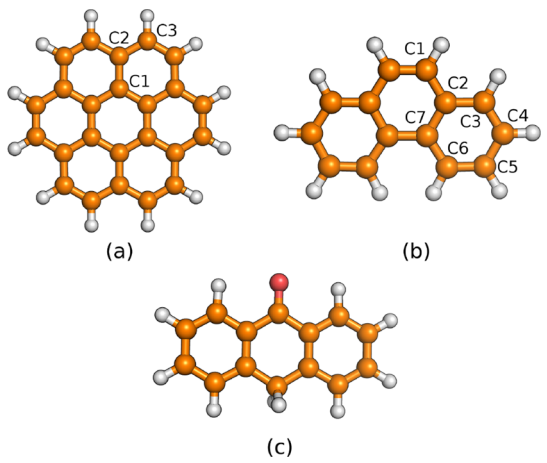

Figure 3. Molecular structures of (a) coronene, (b) phenanthrene, and (c) anthrone. Color code: orange, C; white, H; red, O. The labels indicate chemically nonequivalent carbon atoms.

are computed from KS eigenvalues, the ΔSCF method, and G_0W_0 QP energies. The KS eigenvalues $\{\epsilon_i^{\mathrm{KS}}\}$ and QP excitations $\{\epsilon_i^{G_0W_0}\}$ are related to the binding energies (BEs) for state i by

$$\mathrm{BE}_i^{\mathrm{KS}} = -\epsilon_i^{\mathrm{KS}} \qquad \mathrm{BE}_i^{G_0W_0} = -\epsilon_i^{G_0W_0} \tag{43}$$

In ΔSCF, core-level excitations are computed as the difference between the total energy for the neutral system $E_{\mathrm{tot}}(N)$ and ionized system $E_{\mathrm{tot},i}(N-1)$:

$$\mathrm{BE}_i^{\Delta\mathrm{SCF}} = E_{\mathrm{tot},i}(N-1) - E_{\mathrm{tot}}(N) \tag{44}$$

where N is the number of electrons. For the computation of $E_{\mathrm{tot},i}(N-1)$, one electron is removed from state i and the occupation numbers are constrained accordingly during the SCF cycle.

Except for ΔSCF, all calculations are performed with the FHI-aims program package.[79,96,100] We have obtained the ΔSCF results from the CP2K[101,102] software suite, where the all-electron KS equations are solved in the Gaussian and augmented plane waves (GAPW)[103−105] scheme. Both codes expand the MOs in local basis functions. In GAPW, however, Gaussian-type orbitals are employed instead of NAOs.

All molecular structures have been optimized at the DFT level using NAOs of *tier 2* quality[96] to represent core and valence electrons. The Perdew−Burke−Ernzerhof (PBE)[106] functional is used to model the XC potential, and dispersion interactions are taken into account by employing the Tkatchenko−Scheffler van der Waals correction.[107]

DOI: 10.1021/acs.jctc.8b00458
J. Chem. Theory Comput. XXXX, XXX, XXX−XXX

BEs, self-energy matrix elements $\Sigma_n(\omega)$, and spectral functions $A(\omega)$ have been evaluated using the def2 quadruple-ζ valence plus polarization (def2-QZVP)[108] basis sets. The def2-QZVP basis sets are all-electron basis sets of contracted Gaussian orbitals, which are treated numerically in FHI-aims to be compliant with the NAO scheme. For comparison to experiment, BEs obtained from G_0W_0 have been extrapolated to the complete basis set limit to account for the slow convergence with respect to basis set size previously reported in the literature.[52,53,109−111] Following the procedure described in refs 25 and 52, the extrapolated results are computed from the def2-TZVP and def2-QZVP results by a linear regression against the inverse of the total number of basis functions. Here, def2-TZVP denotes a Gaussian basis set of triple-ζ quality.[108]

BEs from KS eigenvalues and ΔSCF are calculated using the PBE0[112,113] hybrid functional. For G_0W_0, we utilize the PBE-based hybrid (PBEh)[114] functionals with an adjustable fraction α of HF exchange for the underlying DFT calculation. In PBEh(α), the XC energy E_{xc} is given by

$$E_{xc} = \alpha E_x^{EX} + (1-\alpha)E_x^{PBE} + E_c^{PBE} \qquad \alpha \in [0, 1] \tag{45}$$

where E_x^{EX} denotes the HF exchange energy. E_x^{PBE} and E_c^{PBE} are the PBE exchange and correlation energy, respectively. For the evaluation of $\{BE_i^{G_0W_0}\}$, we set $\alpha = 0.5$, which is discussed in section 8.3.

We calculate $\{BE_i^{G_0W_0}\}$ and the spectral functions $A(\omega)$ with our CD approach. We perform AC-G_0W_0 and CD-G_0W_0 calculations to compare self-energy matrix elements. For both approaches, AC-G_0W_0 and CD-G_0W_0, the integrals over the imaginary frequency axis are computed by using a modified Gauss−Legendre grid[79] with 200 grid points. For the analytic continuation, the same set of grid points $\{i\omega\}$ is used to calculate $\Sigma_n^c(i\omega)$, which is fitted to the Padé model.[87] The Padé approximant contains at least 16 parameters. The frequency grid is accordingly increased if more parameters are used.

8. RESULTS AND DISCUSSION

We first discuss numerical parameters of the CD-G_0W_0 approach, the structure of the self-energy and strategies to obtain obtain numerical stable QP solutions for core excitations. The water molecule is used as a representative example for this purpose. We then proceed by comparing core-level BEs of small and larger molecules to experimental data. The computational efficiency of the CD-G_0W_0 approach is finally assessed using acenes as benchmark systems.

8.1. Broadening Parameter η. The CD-G_0W_0 method contains the convergence parameter η; see eqs 33−37. The self-energy is broadened with increasing η, which eventually affects the QP solutions. This is demonstrated in Figure 4a, where the convergence of the BE of the O1s state of H_2O, with respect to η, is displayed. Errors larger than 3 eV are observed for $\eta > 0.5$ a.u. However, the BE converges quickly with η. For $\eta = 0.001$ a.u., the error is $<10^{-4}$ eV. We set this value as the default for the computation of BEs to ensure numerical stability.

The complex parameter $i\eta$ enters the residue term R_n^c in eq 34 and gives rise to a nonzero imaginary part of the self-energy $\mathrm{Im}\Sigma_n^c$ for $\eta \neq 0$. The main contribution to $\mathrm{Im}\Sigma_n^c$ stems from R_n^c. However, $i\eta$ is also present in the integral term I_n^c, i.e., in the denominator of eq 35 and in $\Pi(i\omega)$ (eq 31). Therefore, a minor contribution to $\mathrm{Im}\Sigma_n^c$ is also expected from I_n^c, which has been omitted in previous descriptions of the CD method.[93] This is a fair approximation if only $\mathrm{Re}\Sigma_n^c$ is needed, but neglecting $i\eta$ in I_n^c results in a physical incorrect behavior of the imaginary part. We can easily rationalize this by considering the situation for frequencies ω within the band gap, where $\epsilon_{HOMO} < \omega < \epsilon_{LUMO}$. In the band gap, no poles enter the contour and the residue term vanishes. If I_n^c has only a real part, $\mathrm{Im}\Sigma_n^c$ would be zero. A sudden discontinuity or "step" in $\mathrm{Im}\Sigma_n^c$ then occurs for $\omega = \epsilon_{HOMO}$ and $\omega = \epsilon_{LUMO}$. In fact, such unphysical discontinuities are expected for all frequencies $\omega = \epsilon_n$. This is demonstrated in Figure 4b, where the matrix elements $\mathrm{Im}\Sigma_{1s}^c$ are presented for frequencies in the core region. A discontinuity is observed at $\omega = -510.35$ eV, which corresponds to the first KS eigenvalue ϵ_1. The imaginary part of Σ_n^c becomes smooth when taking the imaginary part of I_n^c into account. This can be explained as follows. Both terms R_n^c and I_n^c have a discontinuity at ϵ_1, which exactly cancels when subtracting I_n^c from R_n^c, such that $\Sigma_n^c = R_n^c - I_n^c$ is smooth; see Figure S1 in the Supporting Information (SI).

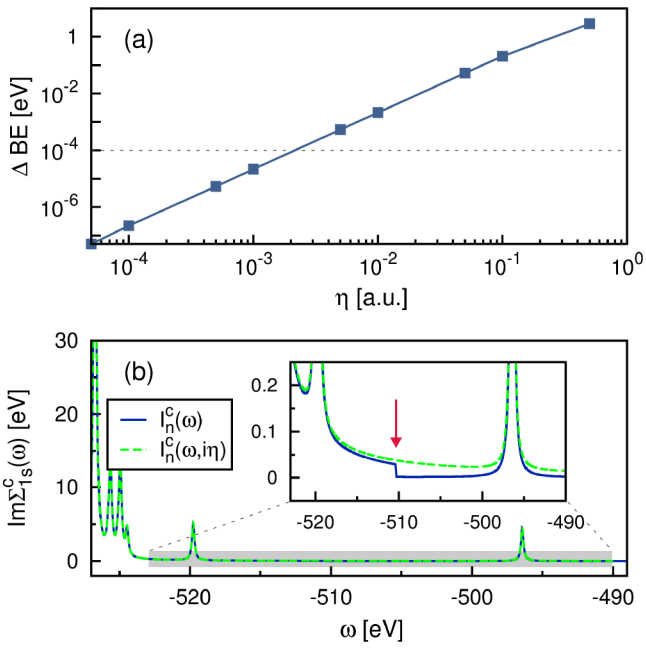

Figure 4. (a) Convergence of the O1s binding energy (BE) of H_2O, with respect to the broadening parameter η. Displayed is the deviation from the BE obtained with $\eta = 1 \times 10^{-6}$ a.u. (b) Imaginary part of the self-energy $\mathrm{Im}\Sigma_{1s}^c = \langle 1s|\mathrm{Im}\Sigma^c(\omega)|1s\rangle$ showing that $i\eta$ must be included in the integral along the imaginary frequency axis I_n^c to avoid "steps" in $\mathrm{Im}\Sigma_n^c(\omega)$. The red arrow indicates the frequency that corresponds to the first KS eigenvalue ϵ_1. ΔBE has been calculated at the PBEh(α = 0.5) level and $\mathrm{Im}\Sigma_{1s}^c(\omega)$ with PBE.

If the imaginary part of I_n^c is neglected, the discontinuities in $\mathrm{Im}\Sigma_n^c$ propagate to the spectral function; see Figure S2 in the SI. These "steps" are hardly visible for small η values, but become very distinct with increasing η. Including $i\eta$ in I_n^c is important when analyzing the spectral function, e.g., integrating the QP peaks. However, it has no measurable effect on the real part $\mathrm{Re}\Sigma_n^c$. We found that a larger grid is required for the numerical integration of the complex integrand. Since the computation of $W_{nm}^c(i\omega)$ is a time-consuming step, we do not include $i\eta$ in I_n^c if only BEs are calculated.

8.2. Structure of the Self-Energy. The precise calculation of the self-energy is essential to obtain correct

DOI: 10.1021/acs.jctc.8b00458
J. Chem. Theory Comput. XXXX, XXX, XXX−XXX

QP energies. In Figure 5, we compare the real self-energy matrix elements $\mathrm{Re}\Sigma_n^c$ obtained from implementations on the

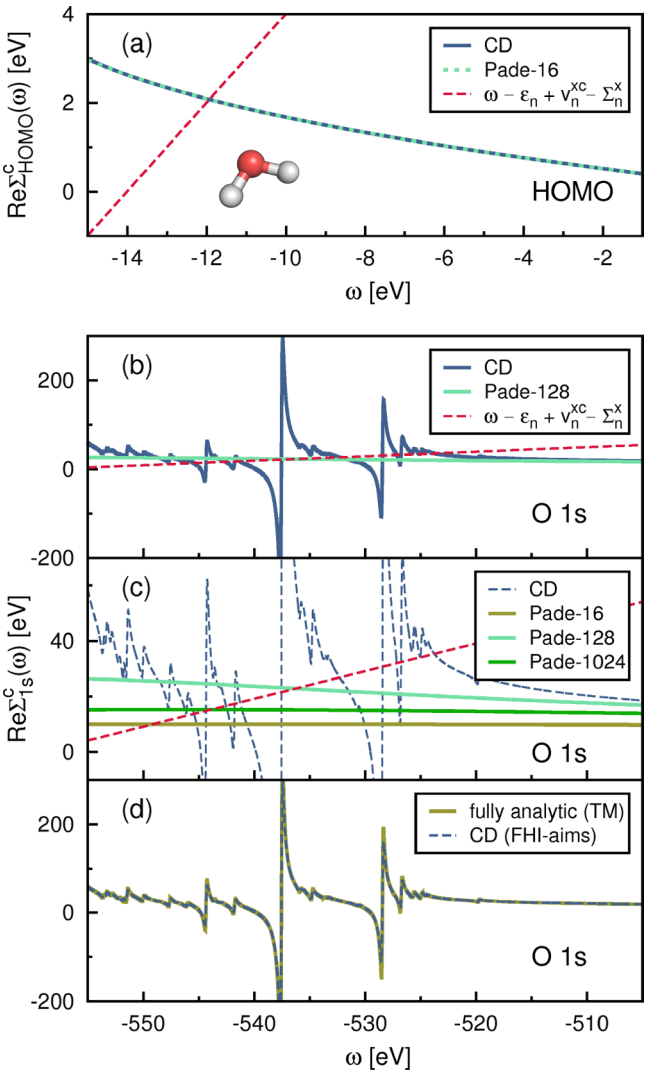

Figure 5. Real part of the self-energy $\Sigma^c(\omega)$ for a single water molecule using PBE as a starting point. Diagonal matrix elements $\mathrm{Re}\Sigma_n^c(\omega) = \langle n|\mathrm{Re}\Sigma^c(\omega)|n\rangle$ for the (a) HOMO and (b) O1s orbital, comparing CD and AC. For the latter, the Padé model with 128 parameters has been used. The intersections with the red dashed lines are the graphical solutions of the QP Equation 1. (c) AC with different numbers of Padé parameters employing a frequency grid of 5000 points. (d) Comparison of $\mathrm{Re}\Sigma_{1s}^c(\omega)$ obtained with our CD-G_0W_0 method and the fully analytic approach implemented in Turbomole (TM).[24]

real and imaginary axis. For the HOMO, AC-G_0W_0 reproduces the CD results accurately with a 16-parameter Padé approximant; see Figure 5a. The self-energy for the HOMO has a smooth structure with a clear single solution for the valence excitations. This is in agreement with previous results presented in the *GW*100 benchmark study[52] reporting a single QP solution for the majority of the systems.

The situation is completely different in the core region. The self-energy for the O1s state displayed in Figure 5b has a complex structure with many poles. Moreover, the self-energy has poles in the region where the QP solutions must be solved, which gives rise to a pronounced multisolution behavior. As shown in Figure 5c, the Padé model fails to reproduce the complicated pole structure. The analytic model function averages, in the best case (128 fit coefficients), roughly through the poles. The QP solution deviates by 13 eV from the exact result, which corresponds to the intersection with the red dashed line at −523.8 eV. Increasing the number of Padé parameters and fit points $\{i\omega\}$ does not necessarily improve the results. The Padé approximant with 1024 parameters represents the self-energy even worse. The error of the corresponding QP solution increases to 20 eV. We can thus conclude that the fitting procedure employed in the AC approach is extremely unstable and unreliable for core states.

To validate the accuracy of the CD approach, we compare our self-energy matrix elements to results from the fully analytic method implemented in Turbomole.[24] The fully analytic method is based on the spectral representation of the reducible response function $\chi(\mathbf{r}, \mathbf{r}', \omega)$, which is explicitly calculated. The screened Coulomb interaction W is then constructed from $\chi(\mathbf{r}, \mathbf{r}', \omega)$ and the self-energy is computed by analytically integrating over G and W. The fully analytic method is also a real-frequency approach, which is numerically stable for any frequency ω of $\Sigma(\omega)$ and contains, except for the broadening η and the basis set, no further parameters. Figure 5d shows that the CD and fully analytic approach yield exactly the same self-energy for the O1s state. The accuracy of our implementation is further confirmed by Figure S3 in the SI, where the N1s matrix elements of acetonitrile are displayed. Also, in this case, we find a perfect agreement. This demonstrates that the CD parameters, e.g., for the numerical integration of I_n^c, are very well under control.

Considering the breakdown of AC-G_0W_0 in the core region, we also expect plasmon−pole models,[68] which represent W by a few poles, to face similar numerical problems. Even though accurate core-level BEs have been obtained for silicon and diamond with a plasmon−pole approximation,[63] the reported deviation from experiment is significantly larger for SiC. This might indicate that numerically precise methods to calculate the self-energy are also required for solid-state systems.

8.3. Identification of the QP Energy. The graphical solution of the QP equation in Figures 5b and 5c shows many intersections with the self-energy. Each of these intersections is a valid solution and, therefore, the identification of the QP solution is not straightforward for core states. When using PBE orbital energies and MOs as starting point, the iterative solution of the QP equation does not converge for any of the systems that we studied. The convergence can be enforced by strongly broadening the self-energy. However, this leads to errors of several eV, as discussed in section 8.1. Circumventing the convergence problem by linearizing the QP equations[85] is not a good strategy either. For the HOMO levels, the linearized version yields very similar QP energies. However, we found deviations of more than 5 eV from the accurate solution for core levels. The large deviations of *GW* core levels from experimental XPS data reported in ref 25 must be partly attributed to the linearization of the QP equation, but also to the choice of the starting point discussed below.

A unique QP solution can be obtained by increasing the amount of exact exchange in the DFT functional. Previous studies for valence excitations showed that PBEh functionals with exact exchange fractions of $\alpha = 0.35$[115] or $\alpha = 0.40$[73] are optimal starting points for the perturbative G_0W_0 approach. We employ the same strategy for core states. Using a hybrid functional as a starting point, the complicated structure of the self-energy remains, but the pole structure is shifted to deeper

DOI: 10.1021/acs.jctc.8b00458
J. Chem. Theory Comput. XXXX, XXX, XXX−XXX

energies and is better separated from the region, where the QP equations are solved. Indeed, for PBEh(α = 0.5), we obtain a clear solution, which is confirmed by the distinct QP peak in the spectral function at −539.30 eV; see Figure 6. This is also

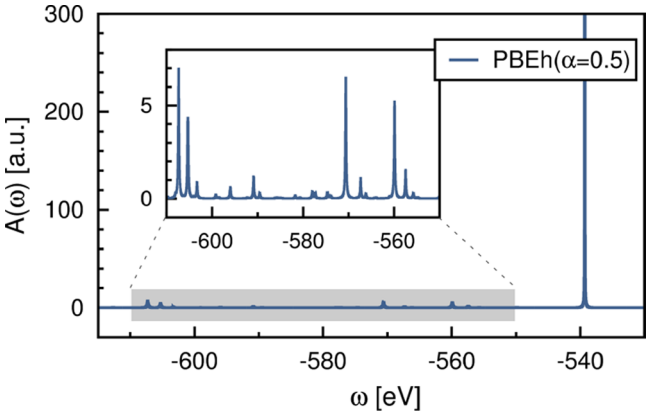

Figure 6. Spectral function $A(\omega)$ of H_2O in the core region using PBEh(α) as starting point for the G_0W_0 calculation. Here, α is defined as the fraction of exact exchange in the PBEh(α) hybrid functional.

reflected in the iterative QP solution, which now converges quickly within 10−15 steps. The number of electrons under the QP peak integrates to 1.43, which adds up to the expected number of 2 when also integrating the satellite spectrum at higher frequencies.

Increasing the amount of exact exchange in the underlying DFT calculation shifts the QP peak to more negative frequencies. These shifts are for core states in the range of a few eV when increasing the α value in PBEh from 0 to 1. Therefore, a careful optimization of the starting point is necessary. For valence states, the α values have been successfully optimized by minimization of the deviation from the straight-line error (DSLE), i.e., the spurious nonlinearity of the total energy as a function of fractional particle numbers.[73] This procedure cannot be transferred to core states because minimizing the DSLE requires a G_0W_0 calculation of the $N-1$ system. Such a calculation is well-defined when removing an electron from the HOMO, but not for core holes. This is evident from eq 7. The irreducible polarizability $\chi_0(\mathbf{r}, \mathbf{r}', \omega)$ contains separate sums over occupied and virtual states, which are no longer defined when the ordering of occupied and virtual states is not consecutive. The strategy for optimizing the starting point for core states requires a detailed assessment of the specific physics at deep energies. This will be presented elsewhere, including a discussion of the satellite spectrum visible in Figure 6. Our first, exploratory study revealed that α values of ∼0.5 are optimal for core excitations, and we use this value in the following.

8.4. Core-Level Binding Energies. Core-level BEs for small molecules with less than 10 atoms are presented in the upper part of Table 1. We focus in the present work on C1s, N1s, and O1s excitations, for which relativistic effects can be neglected. The molecules have been chosen such that different functional groups are included to represent different chemical environments. Note that absolute core-level BEs are discussed in the following.

The BEs obtained from the KS eigenvalues deviate drastically from experiment by up to 17 eV. Large deviations are observed for all three excitation types C1s, N1s, and O1s, which is due to a wrong description of the initial state and the neglect of final state effects, as discussed in length in the

Table 1. Core-Level Binding Energies (BEs), as Obtained from KS Eigenvalues, ΔSCF, and CD-G_0W_0 (in eV) and Deviation from Experiment[a]

		KS		ΔSCF		CD-G_0W_0			
core level	molecule	BE	Δ_{exp}	BE	Δ_{exp}	BE	Δ_{exp}	Exp.	ref_{exp}
C1s	CH_4	277.69	13.16	290.29	0.56	290.77	0.07	290.84	116
	$(CH_3)_2O$	279.32	12.85	291.64	0.53	292.43	0.25	292.17	117
	HCN	279.83	13.7	292.99	0.5	293.29	0.2	293.5	118
N1s	NH_3	390.82	14.70	404.90	0.62	405.36	0.16	405.52	118−120
	HCN	392.20	14.6	406.12	0.7	406.48	0.3	406.8	118, 120, 121
	CH_3NH_2	390.88	14.29	404.48	0.69	405.12	0.05	405.17	118−120
O1s	H_2O	522.74	17.0	538.84	0.9	539.05	0.6	539.7	122
	CH_3OH	522.70	16.18	538.06	0.82	538.55	0.33	538.88	118, 119, 122
	$(CH_3)_2O$	522.82	15.54	537.59	0.77	538.23	0.13	538.36	118, 119, 122
C1s (C1,C2)	coronene	278.85	11.1	289.36	0.5	290.42	0.5	289.9	123
C1s (C3)		278.60	11.0	288.87	0.7	290.11	0.5	289.6	123
C1s (C2,C7)	phenanthrene	278.84	11.4	289.50	0.7	290.71	0.5	290.2	123
C1s (C1,C3−C6)		278.52	11.4	289.20	0.7	290.37	0.5	289.9	123
O1s	anthrone	522.09	14.66	535.31	1.44	536.46	0.29	536.75	124
C1s (C = O)		280.64	12.8	291.96	1.4	293.18	0.2	293.4	124
C1s (C−C,C-H)		278.83	11.89	289.68	1.04	290.72	0.00	290.72	118

[a]Deviation from experiment is defined as $\Delta_{exp} = |BE_i^{theory} - BE_i^{exp}|$. The KS and ΔSCF values have been computed at the PBE0 level. For CD-G_0W_0, PBEh(α = 0.5) is used as starting point, and the BEs have been extrapolated as described in Section 7. The labels for coronene and phenanthrene are given in Figure 3.

DOI: 10.1021/acs.jctc.8b00458
J. Chem. Theory Comput. XXXX, XXX, XXX−XXX

literature.[3,25,29] The absolute BEs obtained from ΔSCF compare much better to experiment with deviations of 0.5−1.0 eV. The ΔSCF values depend significantly on the chosen functional. The PBE0 functional employed in this study is among the functionals that yield the best results in comparison to experiment.[29] However, the error is still too large to properly support the absolute peak assignments in experiment. We obtain the best results with our CD-G_0W_0 method. The deviations are smaller than 0.3 eV for C1s and N1s excitations. Promising results are also found for O1s with deviations of <0.6 eV.

The BEs of large polycyclic molecules with up to 36 atoms are shown in the lower part of Table 1. Note that the ΔSCF values for the molecules with large delocalized π-systems are difficult to compute. The $N-1$ calculations are prone to variational collapses and converging the SCF is a cumbersome task. In addition, the deviation from experiment (1.4 eV) is significantly larger than that observed for the small molecules. CD-G_0W_0, in this case, also yields results that agree favorably with experiment with deviations of <0.5 eV.

A comprehensive assessment of the accuracy of the G_0W_0 method for core levels is beyond the scope of this work. Benchmark studies with more than 60 core excitations will be presented separately.

8.5. Computational Efficiency of CD-G_0W_0. The computational cost, scaling, and parallel performance of our CD-G_0W_0 implementation is evaluated using acenes with 1−13 and 15 rings as representative benchmark systems. Examples of these linearly fused benzene structures are shown in Figure 7a. The execution time, with respect to system size, is reported in Figure 7b at the def2-QZVP level, including the time spent for the DFT calculation. The computationally most expensive steps are the computation of the 3c integrals $(\mu\nu|P)$ and the auxiliary polarization matrices $\Pi(i\omega)$ and $\Pi(|\epsilon_m - \omega|)$.

The evaluation of $(\mu\nu|P)$ over NAOs is the dominating step for small systems up to 42 atoms (~2000 basis functions). The computational cost scales cubically for small systems, but shows an asymptotic quadratic behavior with increasing system size due the sparsity in μ/ν. This reflects in a measured exponent of 2.58. The computation of $\Pi_{PQ}(i\omega)$ is the key step for the computation of the integral term I_n^c and requires $N_\omega N_{occ} N_{virt} N_{aux}^2$ operations, where N_ω is the number of grid points for the integration grid, N_{occ} the number of occupied states, and N_{virt} the number of virtual states. N_{aux} denotes the number of auxiliary functions. Since the size N_ω of the integration grid is independent of the system size, this step scales with $O(N^4)$, which matches the measured exponent. The scaling of $\Pi_{PQ}(|\epsilon_m - \omega|)$ is dependent on the number of residues N_{res} and thus on the excitation type. The number of operations sums up to $N_{res} N_{occ} N_{virt} N_{aux}^2$. For the HOMO, N_{res} is typically one and independent of the system size. However, for core excitations N_{res} equals approximately N_{occ}. Consequently, the number of operations is $O(N^4)$ for valence excitations and increases to $O(N^5)$ for core states, which is one order lower, compared to the fully analytic frequency treatment with $O(N^6)$ complexity.[24] The predicted $O(N^5)$ behavior coincides with the measured exponent of 4.96 for the 1s excitation of the deepest core level. The computation of $\Pi_{PQ}(|\epsilon_m - \omega|)$ starts to dominate the calculation for the system with 2250 basis functions (48 atoms).

The parallel performance of our CD-G_0W_0 implementation is assessed for acenes with 1, 3, 7, and 13 rings in Figure 7c.

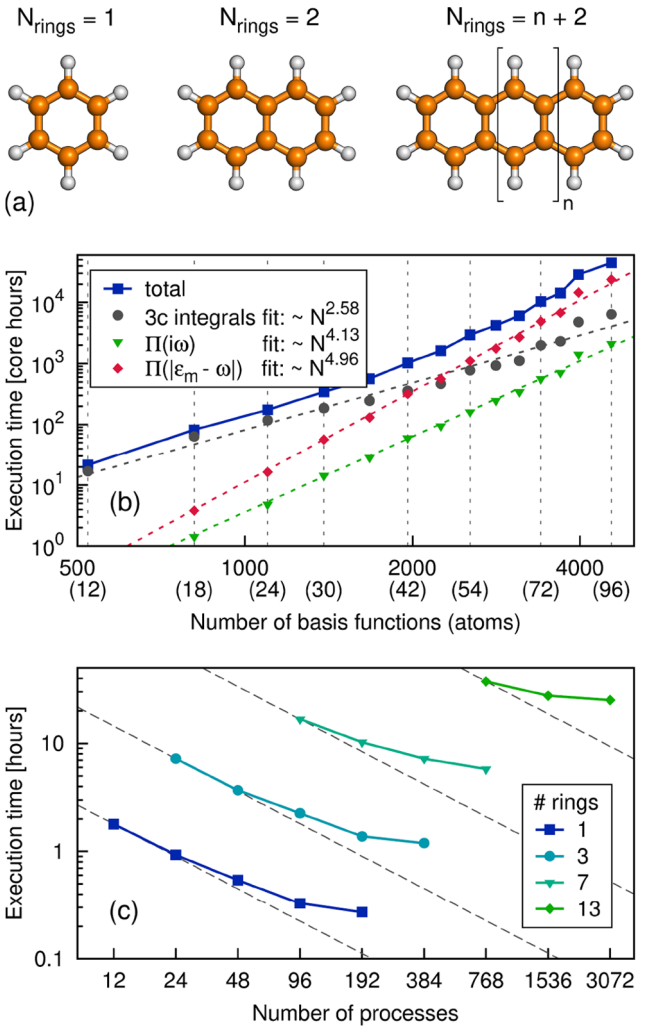

Figure 7. Performance of the CD-G_0W_0 implementation using (a) linear acene structures of 1−13 and 15 rings. The largest system corresponds to 96 atoms. (b) Execution times with respect to system size. Dashed lines represent two-parameter least-squares fits of the prefactor and exponent. The latter is reported in the legend. (c) Scaling test with respect to the number of processes. The gray dashed lines indicate the ideal scaling behavior. Execution times are measured at the def2-QZVP level on a Cray XC40 machine.

The largest system scales well up to 1536 processes with a parallel efficiency of ~70%. With the current implementation, the core-level calculations are feasible for system sizes up to 4500 basis functions or ~100 atoms.

For valence states, the scaling of CD-G_0W_0, with respect to system size, is the same as for RI-V-based AC-G_0W_0 implementations,[53,79] albeit with a slightly larger prefactor. This is due to the fact that $\Pi_{PQ}(|\epsilon_m - \omega|)$ must be evaluated for one or a few residues at each step of the iterative QP scheme. CD-G_0W_0 is the designated method for core and semicore states, but might also be routinely applied with little increase in computational cost for valence excitations.

9. CONCLUSIONS

An efficient, scalable, and numerically accurate G_0W_0 method has been developed for the computation of core excitations. The self-energy Σ is calculated for the full-frequency range on the real axis using the CD technique. Access to the core region is gained by working in a local basis of NAOs in an all-electron

DOI: 10.1021/acs.jctc.8b00458
J. Chem. Theory Comput. XXXX, XXX, XXX−XXX

setup. We combine our scheme with the RI-V approximation to enable an efficient calculation of the 4c-ERIs.

We have shown that the self-energy has a complicated structure with many poles for molecular 1s core states. Our CD-G_0W_0 method computes the self-energy accurately, which is confirmed by comparing to a fully analytic approach. Common G_0W_0 implementations that rely on analytical continuation clearly fail to reproduce the correct frequency dependence of the self-energy for core levels.

Our exploratory studies demonstrate that including a fraction of exact exchange in the underlying DFT calculation is crucial to obtain a distinct QP solution. The PBEh(α = 0.5) functional yields a clear QP peak in the spectral function and has been used to study absolute core-level BEs of small gas-phase molecules. The BEs from CD-G_0W_0 compare favorably to experiment with an error of mostly <0.5 eV and are, in terms of absolute positions, closer to experiment than the DFT-ΔSCF values. Our method reproduces also core-level BEs of large polycyclic molecules within the same error range. The CD-G_0W_0 algorithm is computationally efficient and well parallelized. The current implementation enables core-level calculations for systems up to ∼100 atoms.

The accuracy of G_0W_0 for core states will be more thoroughly assessed for a large benchmark set. However, the present study indicates that the *GW* approach has the potential to become an important computational tool to support the absolute peak assignment in experimental XPS spectra which is already cumbersome for molecules such as phenanthrene and coronene.[123] In addition, it yields interesting insights in the physics and capabilities of *GW* in the core region. This includes starting point effects as well as a further investigation of the obtained satellite spectrum, which might indicate shake-up and shake-down processes. Most importantly, it paves the way for the accurate calculation of core excitations of condensed matter systems, for which ΔSCF approaches cannot be directly applied. Furthermore, the current implementation is a perfect starting point for embedding schemes or fully periodic implementations.

■ ASSOCIATED CONTENT

Supporting Information

The Supporting Information is available free of charge on the ACS Publications website at DOI: 10.1021/acs.jctc.8b00458.

Plot of the residue term R_n^c and the integral term I_n^c for H_2O (Figure S1); spectral function of H_2O with and without $i\eta$ in the integral term I_n^c (Figure S2); self-energy matrix elements for acetonitrile comparing FHI-aims and Turbomole (Figure S3) (PDF)

■ AUTHOR INFORMATION

Corresponding Author

*E-mail: dorothea.golze@aalto.fi.

ORCID

Dorothea Golze: 0000-0002-2196-9350

Michiel J. van Setten: 0000-0003-0557-5260

Present Addresses

[▽]BASF SE, Carl-Bosch-Straße 38, D-67056 Ludwigshafen am Rhein, Germany.

[⊥]IMEC, Kapeldreef 75, B-3001 Leuven, Belgium.

Notes

The authors declare no competing financial interest.

■ ACKNOWLEDGMENTS

We thank the CSC - IT Center for Science for providing computational resources. Calculations were also enabled by the Consortium des Équipements de Calcul Intensif (CÉCI), funded by the Fonds de la Recherche Scientifique de Belgique (F.R.S.-FNRS) under Grant No. 2.5020.11. This work was supported by the Academy of Finland through its Centre of Excellence Programme under Project No. 284621. D. Golze acknowledges financial support by the Swiss National Science Foundation (SNF), Project No. P2ZHP2 168444, and J. Wilhelm acknowledges financial support by the NCCR MARVEL, funded by the SNF.

■ REFERENCES

(1) Barr, T. L. Advances in the Application of X-Ray Photoelectron Spectroscopy (ESCA) Part I. Foundation and Established Methods. *Crit. Rev. Anal. Chem.* **1991**, *22*, 567−635.

(2) Egelhoff, W. F. Core-level binding-energy shifts at surfaces and in solids. *Surf. Sci. Rep.* **1987**, *6*, 253−415.

(3) Bagus, P. S.; Ilton, E. S.; Nelin, C. J. The interpretation of XPS spectra: Insights into materials properties. *Surf. Sci. Rep.* **2013**, *68*, 273−304.

(4) Bagus, P. S.; Illas, F.; Pacchioni, G.; Parmigiani, F. Mechanisms responsible for chemical shifts of core-level binding energies and their relationship to chemical bonding. *J. Electron Spectrosc. Relat. Phenom.* **1999**, *100*, 215−236.

(5) Siegbahn, K.; Nordling, C.; Johansson, G.; Hedman, J.; Hedén, P. F.; Hamrin, K.; Gelius, U.; Bergmark, T.; Werme, L. O.; Manne, R.; Baer, Y. *ESCA Applied to Free Molecules*; North-Holland Publishing Company: Amsterdam, London, 1969; pp 51−136.

(6) Hesse, R.; Chassé, T.; Szargan, R. Peak shape analysis of core level photoelectron spectra using UNIFIT for WINDOWS. *Fresenius' J. Anal. Chem.* **1999**, *365*, 48−54.

(7) Hesse, R.; Chassé, T.; Szargan, R. Unifit 2002−universal analysis software for photoelectron spectra. *Anal. Bioanal. Chem.* **2003**, *375*, 856−863.

(8) van der Heide, P. *X-Ray Photoelectron Spectroscopy: An Introduction to Principles and Practices*; Wiley−Blackwell: Hoboken, NJ, 2011; Chapter 5, pp 101−140.

(9) Pireaux, J. J.; Svensson, S.; Basilier, E.; Malmqvist, P.-Å.; Gelius, U.; Caudano, R.; Siegbahn, K. Core-electron relaxation energies and valence-band formation of linear alkanes studied in the gas phase by means of electron spectroscopy. *Phys. Rev. A: At., Mol., Opt. Phys.* **1976**, *14*, 2133−2145.

(10) Carravetta, V.; Iucci, G.; Ferri, A.; Russo, M. V.; Stranges, S.; de Simone, M.; Polzonetti, G. Synchrotron radiation photoemission study of some π-conjugated alkynes in the gas phase: Experiment and theory. *Chem. Phys.* **2001**, *264*, 175−186.

(11) de Brito, A. N.; Svensson, S.; Ågren, H.; Delhalle, J. Experimental and theoretical study of the XPS core levels of gas phase acetonitrile, acrylonitrile and propionitrile. Model molecules for polyacrylonitrile. *J. Electron Spectrosc. Relat. Phenom.* **1993**, *63*, 239−251.

(12) Hohenberg, P.; Kohn, W. Inhomogeneous Electron Gas. *Phys. Rev.* **1964**, *136*, B864−B871.

(13) Kohn, W.; Sham, L. J. Self-Consistent Equations Including Exchange and Correlation Effects. *Phys. Rev.* **1965**, *140*, A1133−A1138.

(14) Hedin, L. On correlation effects in electron spectroscopies and the *GW* approximation. *J. Phys.: Condens. Matter* **1999**, *11*, R489−R528.

(15) Sham, L. J.; Schlüter, M. Density-functional theory of the band gap. *Phys. Rev. B: Condens. Matter Mater. Phys.* **1985**, *32*, 3883−3889.

(16) Yang, L.; Park, C.-H.; Son, Y.-W.; Cohen, M. L.; Louie, S. G. Quasiparticle Energies and Band Gaps in Graphene Nanoribbons. *Phys. Rev. Lett.* **2007**, *99*, 186801.

DOI: 10.1021/acs.jctc.8b00458
J. Chem. Theory Comput. XXXX, XXX, XXX−XXX

(17) Blase, X.; Attaccalite, C.; Olevano, V. First-principles *GW* calculations for fullerenes, porphyrins, phtalocyanine, and other molecules of interest for organic photovoltaic applications. *Phys. Rev. B: Condens. Matter Mater. Phys.* **2011**, *83*, 115103.
(18) Ke, S.-H. All-electron *GW* methods implemented in molecular orbital space: Ionization energy and electron affinity of conjugated molecules. *Phys. Rev. B: Condens. Matter Mater. Phys.* **2011**, *84*, 205415.
(19) Almbladh, C.-O.; von Barth, U. Exact results for the charge and spin densities, exchange-correlation potentials, and density-functional eigenvalues. *Phys. Rev. B: Condens. Matter Mater. Phys.* **1985**, *31*, 3231−3244.
(20) Levy, M.; Perdew, J. P.; Sahni, V. Exact differential equation for the density and ionization energy of a many-particle system. *Phys. Rev. A: At., Mol., Opt. Phys.* **1984**, *30*, 2745−2748.
(21) Stowasser, R.; Hoffmann, R. What Do the Kohn-Sham Orbitals and Eigenvalues Mean? *J. Am. Chem. Soc.* **1999**, *121*, 3414−3420.
(22) Baerends, E. J.; Gritsenko, O. V. A Quantum Chemical View of Density Functional Theory. *J. Phys. Chem. A* **1997**, *101*, 5383−5403.
(23) Koopmans, T. Über die Zuordnung von Wellenfunktionen und Eigenwerten zu den Einzelnen Elektronen Eines Atoms. *Physica* **1934**, *1*, 104−113.
(24) van Setten, M. J.; Weigend, F.; Evers, F. The *GW*-Method for Quantum Chemistry Applications: Theory and Implementation. *J. Chem. Theory Comput.* **2013**, *9*, 232−246.
(25) van Setten, M. J.; Costa, R.; Viñes, F.; Illas, F. Assessing *GW* Approaches for Predicting Core Level Binding Energies. *J. Chem. Theory Comput.* **2018**, *14*, 877−883.
(26) Bagus, P. S. Self-Consistent-Field Wave Functions for Hole States of Some Ne-Like and Ar-Like Ions. *Phys. Rev.* **1965**, *139*, A619−A634.
(27) Viñes, F.; Sousa, C.; Illas, F. On the prediction of core level binding energies in molecules, surfaces and solids. *Phys. Chem. Chem. Phys.* **2018**, *20*, 8403−8410.
(28) Pueyo Bellafont, N.; Álvarez Saiz, G.; Viñes, F.; Illas, F. Performance of Minnesota functionals on predicting core-level binding energies of molecules containing main-group elements. *Theor. Chem. Acc.* **2016**, *135*, 35.
(29) Pueyo Bellafont, N.; Bagus, P. S.; Illas, F. Prediction of core level binding energies in density functional theory: Rigorous definition of initial and final state contributions and implications on the physical meaning of Kohn-Sham energies. *J. Chem. Phys.* **2015**, *142*, 214102.
(30) Boman, M.; Åagren, H.; Stafström, S. A Delta Self-Consistent-Field Study of Core Electron Binding Energies of Model Molecules for the Aluminum/Polythiophene Interface. *J. Phys. Chem.* **1995**, *99*, 16597−16601.
(31) Bagus, P. S.; Coolbaugh, D.; Kowalczyk, S.; Pacchioni, G.; Parmigiani, F. Molecular orbital theory for the analysis of photoemission spectra. *J. Electron Spectrosc. Relat. Phenom.* **1990**, *51*, 69−74.
(32) Ågren, H.; Bagus, P. S.; Roos, B. O. Symmetry adapted versus symmetry broken wavefunctions: the 1s core level ions of O_2^+. *Chem. Phys. Lett.* **1981**, *82*, 505−510.
(33) Bagus, P. S.; Schaefer, H. F., III Localized and Delocalized 1s Hole States of the O_2^+ Molecular Ion. *J. Chem. Phys.* **1972**, *56*, 224−226.
(34) Hedin, L.; Johansson, A. Polarization corrections to core levels. *J. Phys. B: At. Mol. Phys.* **1969**, *2*, 1336−1346.
(35) Pehlke, E.; Scheffler, M. Evidence for site-sensitive screening of core holes at the Si and Ge (001) surface. *Phys. Rev. Lett.* **1993**, *71*, 2338−2341.
(36) Köhler, L.; Kresse, G. Density functional study of CO on Rh(111). *Phys. Rev. B: Condens. Matter Mater. Phys.* **2004**, *70*, 165405.
(37) Pueyo Bellafont, N.; Viñes, F.; Hieringer, W.; Illas, F. Predicting core level binding energies shifts: Suitability of the projector augmented wave approach as implemented in VASP. *J. Comput. Chem.* **2017**, *38*, 518−522.
(38) Reining, L. The *GW* approximation: content, successes and limitations. *WIREs Comput. Mol. Sci.* **2018**, *8*, e1344.
(39) Hedin, L. New Method for Calculating the One-Particle Green's Function with Application to the Electron-Gas Problem. *Phys. Rev.* **1965**, *139*, A796−A823.
(40) Rinke, P.; Qteish, A.; Neugebauer, J.; Freysoldt, C.; Scheffler, M. Combining *GW* calculations with exact-exchange density-functional theory: an analysis of valence-band photoemission for compound semiconductors. *New J. Phys.* **2005**, *7*, 126.
(41) Rinke, P.; Janotti, A.; Scheffler, M.; Van de Walle, C. G. Defect Formation Energies without the Band-Gap Problem: Combining Density-Functional Theory and the *GW* Approach for the Silicon Self-Interstitial. *Phys. Rev. Lett.* **2009**, *102*, 026402.
(42) Liao, P.; Carter, E. A. Testing variations of the *GW* approximation on strongly correlated transition metal oxides: hematite (α-Fe_2O_3) as a benchmark. *Phys. Chem. Chem. Phys.* **2011**, *13*, 15189−15199.
(43) Berger, J. A.; Reining, L.; Sottile, F. Ab initio calculations of electronic excitations: Collapsing spectral sums. *Phys. Rev. B: Condens. Matter Mater. Phys.* **2010**, *82*, 041103.
(44) Berger, J. A.; Reining, L.; Sottile, F. Efficient *GW* calculations for SnO_2, ZnO, and rubrene: The effective-energy technique. *Phys. Rev. B: Condens. Matter Mater. Phys.* **2012**, *85*, 085126.
(45) Rinke, P.; Schleife, A.; Kioupakis, E.; Janotti, A.; Rödl, C.; Bechstedt, F.; Scheffler, M.; Van de Walle, C. G. First-Principles Optical Spectra for F Centers in MgO. *Phys. Rev. Lett.* **2012**, *108*, 126404.
(46) Klimeš, J.; Kaltak, M.; Kresse, G. Predictive *GW* calculations using plane waves and pseudopotentials. *Phys. Rev. B: Condens. Matter Mater. Phys.* **2014**, *90*, 075125.
(47) Förster, T.; Krüger, P.; Rohlfing, M. Two-dimensional topological phases and electronic spectrum of Bi_2Se_3 thin films from *GW* calculations. *Phys. Rev. B: Condens. Matter Mater. Phys.* **2015**, *92*, 201404.
(48) Förster, T.; Krüger, P.; Rohlfing, M. *GW* calculations for Bi_2Te_3 and Sb_2Te_3 thin films: Electronic and topological properties. *Phys. Rev. B: Condens. Matter Mater. Phys.* **2016**, *93*, 205442.
(49) Chen, W.; Pasquarello, A. Accuracy of *GW* for calculating defect energy levels in solids. *Phys. Rev. B: Condens. Matter Mater. Phys.* **2017**, *96*, 020101.
(50) Wilhelm, J.; Hutter, J. Periodic *GW* calculations in the Gaussian and plane-waves scheme. *Phys. Rev. B: Condens. Matter Mater. Phys.* **2017**, *95*, 235123.
(51) Scherpelz, P.; Govoni, M.; Hamada, I.; Galli, G. Implementation and Validation of Fully Relativistic *GW* Calculations: Spin-Orbit Coupling in Molecules, Nanocrystals, and Solids. *J. Chem. Theory Comput.* **2016**, *12*, 3523−3544.
(52) van Setten, M. J.; Caruso, F.; Sharifzadeh, S.; Ren, X.; Scheffler, M.; Liu, F.; Lischner, J.; Lin, L.; Deslippe, J. R.; Louie, S. G.; Yang, C.; Weigend, F.; Neaton, J. B.; Evers, F.; Rinke, P. *GW*100: Benchmarking G_0W_0 for Molecular Systems. *J. Chem. Theory Comput.* **2015**, *11*, 5665−5687.
(53) Wilhelm, J.; Del Ben, M.; Hutter, J. *GW* in the Gaussian and Plane Waves Scheme with Application to Linear Acenes. *J. Chem. Theory Comput.* **2016**, *12*, 3623−3635.
(54) Govoni, M.; Galli, G. *GW*100: Comparison of Methods and Accuracy of Results Obtained with the WEST Code. *J. Chem. Theory Comput.* **2018**, *14*, 1895−1909.
(55) Kühn, M.; Weigend, F. One-Electron Energies from the Two-Component *GW* Method. *J. Chem. Theory Comput.* **2015**, *11*, 969−979.
(56) Gui, X.; Holzer, C.; Klopper, W. Accuracy Assessment of *GW* Starting Points for Calculating Molecular Excitation Energies Using the Bethe-Salpeter Formalism. *J. Chem. Theory Comput.* **2018**, *14*, 2127−2136.
(57) Hung, L.; Bruneval, F.; Baishya, K.; Öğüt, S. Benchmarking the *GW* Approximation and Bethe-Salpeter Equation for Groups IB and IIB Atoms and Monoxides. *J. Chem. Theory Comput.* **2017**, *13*, 2135−2146.

DOI: 10.1021/acs.jctc.8b00458
J. Chem. Theory Comput. XXXX, XXX, XXX−XXX

(58) Maggio, E.; Liu, P.; van Setten, M. J.; Kresse, G. *GW*100: A Plane Wave Perspective for Small Molecules. *J. Chem. Theory Comput.* **2017**, *13*, 635−648.
(59) van Setten, M. J.; Giantomassi, M.; Gonze, X.; Rignanese, G.-M.; Hautier, G. Automation methodologies and large-scale validation for *GW*: Towards high-throughput *GW* calculations. *Phys. Rev. B: Condens. Matter Mater. Phys.* **2017**, *96*, 155207.
(60) Gallandi, L.; Marom, N.; Rinke, P.; Körzdörfer, T. Accurate Ionization Potentials and Electron Affinities of Acceptor Molecules II: Non-Empirically Tuned Long-Range Corrected Hybrid Functionals. *J. Chem. Theory Comput.* **2016**, *12*, 605−614.
(61) Knight, J. W.; Wang, X.; Gallandi, L.; Dolgounitcheva, O.; Ren, X.; Ortiz, J. V.; Rinke, P.; Körzdörfer, T.; Marom, N. Accurate Ionization Potentials and Electron Affinities of Acceptor Molecules III: A Benchmark of *GW* Methods. *J. Chem. Theory Comput.* **2016**, *12*, 615−626.
(62) Gallandi, L.; Körzdörfer, T. Long-Range Corrected DFT Meets *GW*: Vibrationally Resolved Photoelectron Spectra from First Principles. *J. Chem. Theory Comput.* **2015**, *11*, 5391−5400.
(63) Ishii, S.; Iwata, S.; Ohno, K. All-Electron *GW* Calculations of Silicon, Diamond, and Silicon Carbide. *Mater. Trans.* **2010**, *51*, 2150−2156.
(64) Aoki, T.; Ohno, K. Accurate quasiparticle calculation of x-ray photoelectron spectra of solids. *J. Phys.: Condens. Matter* **2018**, *30*, 21LT01.
(65) Deslippe, J.; Samsonidze, G.; Strubbe, D. A.; Jain, M.; Cohen, M. L.; Louie, S. G. Berkeley*GW*: A massively parallel computer package for the calculation of the quasiparticle and optical properties of materials and nanostructures. *Comput. Phys. Commun.* **2012**, *183*, 1269−1289.
(66) Marini, A.; Hogan, C.; Grüning, M.; Varsano, D. yambo: An ab initio tool for excited state calculations. *Comput. Phys. Commun.* **2009**, *180*, 1392−1403.
(67) Liu, P.; Kaltak, M.; Klimeš, J.; Kresse, G. Cubic scaling *GW*: Towards fast quasiparticle calculations. *Phys. Rev. B: Condens. Matter Mater. Phys.* **2016**, *94*, 165109.
(68) Aryasetiawan, F.; Gunnarsson, O. The *GW* method. *Rep. Prog. Phys.* **1998**, *61*, 237−312.
(69) Adler, S. L. Quantum Theory of the Dielectric Constant in Real Solids. *Phys. Rev.* **1962**, *126*, 413−420.
(70) Wiser, N. Dielectric Constant with Local Field Effects Included. *Phys. Rev.* **1963**, *129*, 62−69.
(71) Marom, N.; Caruso, F.; Ren, X.; Hofmann, O. T.; Körzdörfer, T.; Chelikowsky, J. R.; Rubio, A.; Scheffler, M.; Rinke, P. Benchmark of *GW* methods for azabenzenes. *Phys. Rev. B: Condens. Matter Mater. Phys.* **2012**, *86*, 245127.
(72) Körzdörfer, T.; Marom, N. Strategy for finding a reliable starting point for G_0W_0 demonstrated for molecules. *Phys. Rev. B: Condens. Matter Mater. Phys.* **2012**, *86*, 041110.
(73) Dauth, M.; Caruso, F.; Kümmel, S.; Rinke, P. Piecewise linearity in the *GW* approximation for accurate quasiparticle energy predictions. *Phys. Rev. B: Condens. Matter Mater. Phys.* **2016**, *93*, 121115.
(74) Vahtras, O.; Almlöf, J.; Feyereisen, M. W. Integral approximations for LCAO-SCF calculations. *Chem. Phys. Lett.* **1993**, *213*, 514−518.
(75) Weigend, F. A fully direct RI-HF algorithm: Implementation, optimized auxiliary basis sets, demonstration of accuracy and efficiency. *Phys. Chem. Chem. Phys.* **2002**, *4*, 4285−4291.
(76) Weigend, F. Accurate Coulomb-fitting basis sets for H to Rn. *Phys. Chem. Chem. Phys.* **2006**, *8*, 1057−1065.
(77) Eichkorn, K.; Treutler, O.; Öhm, H.; Häser, M.; Ahlrichs, R. Auxiliary basis sets to approximate Coulomb potentials. *Chem. Phys. Lett.* **1995**, *240*, 283−290.
(78) Duchemin, I.; Li, J.; Blase, X. Hybrid and Constrained Resolution-of-Identity Techniques for Coulomb Integrals. *J. Chem. Theory Comput.* **2017**, *13*, 1199−1208.
(79) Ren, X.; Rinke, P.; Blum, V.; Wieferink, J.; Tkatchenko, A.; Sanfilippo, A.; Reuter, K.; Scheffler, M. Resolution-of-identity approach to Hartree-Fock, hybrid density functionals, RPA, MP2 and *GW* with numeric atom-centered orbital basis functions. *New J. Phys.* **2012**, *14*, 053020.
(80) Bruneval, F.; Rangel, T.; Hamed, S. M.; Shao, M.; Yang, C.; Neaton, J. B. MOLGW1: Many-body perturbation theory software for atoms, molecules, and clusters. *Comput. Phys. Commun.* **2016**, *208*, 149−161.
(81) Dunlap, B. I.; Connolly, J. W. D.; Sabin, J. R. On some approximations in applications of Xα theory. *J. Chem. Phys.* **1979**, *71*, 3396−3402.
(82) Merlot, P.; Kjærgaard, T.; Helgaker, T.; Lindh, R.; Aquilante, F.; Reine, S.; Pedersen, T. B. Attractive electron-electron interactions within robust local fitting approximations. *J. Comput. Chem.* **2013**, *34*, 1486−1496.
(83) Golze, D.; Iannuzzi, M.; Hutter, J. Local Fitting of the Kohn-Sham Density in a Gaussian and Plane Waves Scheme for Large-Scale Density Functional Theory Simulations. *J. Chem. Theory Comput.* **2017**, *13*, 2202−2214.
(84) Rieger, M. M.; Steinbeck, L.; White, I. D.; Rojas, H. N.; Godby, R. W. The *GW* space-time method for the self-energy of large systems. *Comput. Phys. Commun.* **1999**, *117*, 211−228.
(85) Giantomassi, M.; Stankovski, M.; Shaltaf, R.; Grüning, M.; Bruneval, F.; Rinke, P.; Rignanese, G.-M. Electronic properties of interfaces and defects from many-body perturbation theory: Recent developments and applications. *Phys. Status Solidi B* **2011**, *248*, 275−289.
(86) Wilhelm, J.; Golze, D.; Talirz, L.; Hutter, J.; Pignedoli, C. A. Toward *GW* Calculations on Thousands of Atoms. *J. Phys. Chem. Lett.* **2018**, *9*, 306−312.
(87) Vidberg, H. J.; Serene, J. W. Solving the Eliashberg equations by means of N-point Padé approximants. *J. Low Temp. Phys.* **1977**, *29*, 179−192.
(88) Caruso, F.; Rinke, P.; Ren, X.; Rubio, A.; Scheffler, M. Self-consistent *GW*: All-electron implementation with localized basis functions. *Phys. Rev. B: Condens. Matter Mater. Phys.* **2013**, *88*, 075105.
(89) Friedrich, C.; Blügel, S.; Schindlmayr, A. Efficient implementation of the *GW* approximation within the all-electron FLAPW method. *Phys. Rev. B: Condens. Matter Mater. Phys.* **2010**, *81*, 125102.
(90) Pham, T. A.; Nguyen, H.-V.; Rocca, D.; Galli, G. *GW* calculations using the spectral decomposition of the dielectric matrix: Verification, validation, and comparison of methods. *Phys. Rev. B: Condens. Matter Mater. Phys.* **2013**, *87*, 155148.
(91) Godby, R. W.; Schlüter, M.; Sham, L. J. Self-energy operators and exchange-correlation potentials in semiconductors. *Phys. Rev. B: Condens. Matter Mater. Phys.* **1988**, *37*, 10159−10175.
(92) Lebègue, S.; Arnaud, B.; Alouani, M.; Bloechl, P. E. Implementation of an all-electron *GW* approximation based on the projector augmented wave method without plasmon pole approximation: Application to Si, SiC, AlAs, InAs, NaH, and KH. *Phys. Rev. B: Condens. Matter Mater. Phys.* **2003**, *67*, 155208.
(93) Bruneval, F. Exchange and Correlation in the Electronic Structure of Solids from Silicon to Cuprous Oxide: *GW* Approximation and Beyond. Ph.D. Thesis, Ecole Polytechnique, Palaiseau, France, 2005 (available via the Internet at: https://etsf.polytechnique.fr/node/1670).
(94) Gonze, X.; Amadon, B.; Anglade, P.-M.; Beuken, J.-M.; Bottin, F.; Boulanger, P.; Bruneval, F.; Caliste, D.; Caracas, R.; Côté, M.; Deutsch, T.; Genovese, L.; Ghosez, P.; Giantomassi, M.; Goedecker, S.; Hamann, D. R.; Hermet, P.; Jollet, F.; Jomard, G.; Leroux, S.; Mancini, M.; Mazevet, S.; Oliveira, M. J. T.; Onida, G.; Pouillon, Y.; Rangel, T.; Rignanese, G.-M.; Sangalli, D.; Shaltaf, R.; Torrent, M.; Verstraete, M. J.; Zerah, G.; Zwanziger, J. W. ABINIT: First-principles approach to material and nanosystem properties. *Comput. Phys. Commun.* **2009**, *180*, 2582−2615.
(95) Govoni, M.; Galli, G. Large Scale *GW* Calculations. *J. Chem. Theory Comput.* **2015**, *11*, 2680−2696.
(96) Blum, V.; Gehrke, R.; Hanke, F.; Havu, P.; Havu, V.; Ren, X.; Reuter, K.; Scheffler, M. Ab initio molecular simulations with numeric

DOI: 10.1021/acs.jctc.8b00458
J. Chem. Theory Comput. XXXX, XXX, XXX−XXX

atom-centered orbitals. *Comput. Phys. Commun.* **2009**, *180*, 2175−2196.
(97) Talman, J. D. Numerical calculation of four-center Coulomb integrals. *J. Chem. Phys.* **1984**, *80*, 2000−2008.
(98) Talman, J. D. Numerical methods for multicenter integrals for numerically defined basis functions applied in molecular calculations. *Int. J. Quantum Chem.* **2003**, *93*, 72−90.
(99) Talman, J. D. NumSBT: A subroutine for calculating spherical Bessel transforms numerically. *Comput. Phys. Commun.* **2009**, *180*, 332−338.
(100) Havu, V.; Blum, V.; Havu, P.; Scheffler, M. Efficient integration for all-electron electronic structure calculation using numeric basis functions. *J. Comput. Phys.* **2009**, *228*, 8367−8379.
(101) Hutter, J.; Iannuzzi, M.; Schiffmann, F.; VandeVondele, J. CP2K: atomistic simulations of condensed matter systems. *WIREs Comput. Mol. Sci.* **2014**, *4*, 15−25.
(102) The CP2K developers group, CP2K is freely available via the Internet at: http://www.cp2k.org/ (accessed February, 2018).
(103) Lippert, G.; Hutter, J.; Parrinello, M. The Gaussian and augmented-plane-wave density functional method for ab initio molecular dynamics simulations. *Theor. Chem. Acc.* **1999**, *103*, 124−140.
(104) Krack, M.; Parrinello, M. All-electron ab-initio molecular dynamics. *Phys. Chem. Chem. Phys.* **2000**, *2*, 2105−2112.
(105) Iannuzzi, M.; Hutter, J. Inner-shell spectroscopy by the Gaussian and augmented plane wave method. *Phys. Chem. Chem. Phys.* **2007**, *9*, 1599−1610.
(106) Perdew, J. P.; Burke, K.; Ernzerhof, M. Generalized Gradient Approximation Made Simple. *Phys. Rev. Lett.* **1996**, *77*, 3865−3868.
(107) Tkatchenko, A.; Scheffler, M. Accurate Molecular Van Der Waals Interactions from Ground-State Electron Density and Free-Atom Reference Data. *Phys. Rev. Lett.* **2009**, *102*, 073005.
(108) Weigend, F.; Ahlrichs, R. Balanced basis sets of split valence, triple zeta valence and quadruple zeta valence quality for H to Rn: Design and assessment of accuracy. *Phys. Chem. Chem. Phys.* **2005**, *7*, 3297−3305.
(109) Bruneval, F. Ionization energy of atoms obtained from *GW* self-energy or from random phase approximation total energies. *J. Chem. Phys.* **2012**, *136*, 194107.
(110) Bruneval, F.; Marques, M. A. L. Benchmarking the Starting Points of the *GW* Approximation for Molecules. *J. Chem. Theory Comput.* **2013**, *9*, 324−329.
(111) Jacquemin, D.; Duchemin, I.; Blase, X. Benchmarking the Bethe-Salpeter Formalism on a Standard Organic Molecular Set. *J. Chem. Theory Comput.* **2015**, *11*, 3290−3304.
(112) Adamo, C.; Barone, V. Toward reliable density functional methods without adjustable parameters: The PBE0 model. *J. Chem. Phys.* **1999**, *110*, 6158−6170.
(113) Ernzerhof, M.; Scuseria, G. E. Assessment of the Perdew-Burke-Ernzerhof exchange-correlation functional. *J. Chem. Phys.* **1999**, *110*, 5029−5036.
(114) Atalla, V.; Yoon, M.; Caruso, F.; Rinke, P.; Scheffler, M. Hybrid density functional theory meets quasiparticle calculations: A consistent electronic structure approach. *Phys. Rev. B: Condens. Matter Mater. Phys.* **2013**, *88*, 165122.
(115) Caruso, F.; Dauth, M.; van Setten, M. J.; Rinke, P. Benchmark of *GW* Approaches for the *GW*100 Test Set. *J. Chem. Theory Comput.* **2016**, *12*, 5076−5087.
(116) Myrseth, V.; Bozek, J. D.; Kukk, E.; Sæthre, L. J.; Thomas, T. D. Adiabatic and vertical carbon 1s ionization energies in representative small molecules. *J. Electron Spectrosc. Relat. Phenom.* **2002**, *122*, 57−63.
(117) Drake, J. E.; Riddle, C.; Henderson, H. E.; Glavinčevski, B. ESCA investigations of Group IV derivatives. Part III. Binding energies for methyl substituted disilyl and digermyl chalcogenide series. *Can. J. Chem.* **1977**, *55*, 2957−2961.
(118) Bakke, A. A.; Chen, H.-W.; Jolly, W. L. A table of absolute core-electron binding-energies for gaseous atoms and molecules. *J. Electron Spectrosc. Relat. Phenom.* **1980**, *20*, 333−366.
(119) Mills, B. E.; Martin, R. L.; Shirley, D. A. Further studies of the core binding energy-proton affinity correlation in molecules. *J. Am. Chem. Soc.* **1976**, *98*, 2380−2385.
(120) Thomas, T. D.; Shaw, R. W. Accurate core ionization potentials and photoelectron kinetic energies for light elements. *J. Electron Spectrosc. Relat. Phenom.* **1974**, *5*, 1081−1094.
(121) Finn, P.; Pearson, R. K.; Hollander, J. M.; Jolly, W. L. Chemical shifts in core electron binding energies for some gaseous nitrogen compounds. *Inorg. Chem.* **1971**, *10*, 378−381.
(122) Siegbahn, K.; Nordling, C.; Johansson, G.; Hedman, J.; Hedén, P. F.; Hamrin, K.; Gelius, U.; Bergmark, T.; Werme, L. O.; Manne, R.; Baer, Y. *ESCA Applied to Free Molecules*; North-Holland Publishing Company: Amsterdam, London, 1969; p 12.
(123) Fronzoni, G.; Baseggio, O.; Stener, M.; Hua, W.; Tian, G.; Luo, Y.; Apicella, B.; Alfé, M.; de Simone, M.; Kivimäki, A.; Coreno, M. Vibrationally resolved high-resolution NEXAFS and XPS spectra of phenanthrene and coronene. *J. Chem. Phys.* **2014**, *141*, 044313.
(124) Jolly, W. L.; Schaaf, T. F. π-Donor relaxation in the oxygen 1s ionization of carbonyl compounds. *J. Am. Chem. Soc.* **1976**, *98*, 3178−3181.

DOI: 10.1021/acs.jctc.8b00458
J. Chem. Theory Comput. XXXX, XXX, XXX−XXX